# $Zn_2GeO_4$ and $Zn_2SnO_4$ Nanowires for High-Capacity Lithium- and Sodium-Ion Batteries

Received 00th January 20xx,
Accepted 00th January 20xx

DOI: 10.1039/x0xx00000x

www.rsc.org/

Young Rok Lim,[a] Chan Su Jung,[a] Hyung Soon Im,[a] Kidong Park,[a] Jeunghee Park,*[a] Won Il Cho*[b] and Eun Hee Cha*[c]

Germanium (Ge) and tin (Sn) are considered to be the most promising alternatives to commercial carbon materials in lithium- and sodium-ion batteries. High-purity zinc germanium oxide ($Zn_2GeO_4$) and zinc tin oxide ($Zn_2SnO_4$) nanowires were synthesized using a hydrothermal method, and their electrochemical properties as anode materials in lithium- and sodium-ion batteries were comparatively investigated. The nanowires had a uniform morphology and consisted of single-crystalline rhombohedral ($Zn_2GeO_4$) and cubic ($Zn_2SnO_4$) phases. For lithium ion batteries, $Zn_2GeO_4$ and $Zn_2SnO_4$ showed an excellent cycling performance, with a capacity of 1220 and 983 mA h $g^{-1}$ after 100 cycles, respectively. Their high capacities are attributed to a combination of the alloy formation reaction of Zn and Ge (or Sn) with Li, and the conversion reaction: $ZnO + 2Li^+ + 2e^- \leftrightarrow Zn + Li_2O$ and $GeO_2$ (or $SnO_2$) $+ 4Li^+ + 4e^- \leftrightarrow$ Ge (or Sn) $+ 2Li_2O$. For the first time, we examined the cycling performance of $Zn_2GeO_4$ and $Zn_2SnO_4$ in sodium ion batteries; their capacities were 342 mA h $g^{-1}$ and 306 mA h $g^{-1}$ after 100 cycles, respectively. The capacity of $Zn_2SnO_4$ is much higher than the theoretical capacity (100 mA h $g^{-1}$), while that of $Zn_2SnO_4$ is close to the theoretical capacity (320 mA h $g^{-1}$). We suggest a contribution of the conversion reaction in increasing the capacities, which is similar to the case of lithium ion batteries. The present systematic comparison between the lithiation and sodiation will provide valuable information for the development of high-performance lithium- and sodium-ion batteries.

## Introduction

With growing concerns about global warming and the fast depletion of fossil fuels, it is of great demand to develop clean and renewable energy resources. So far, tremendous efforts have been devoted to improving the energy and power density of electric energy storage devices such as rechargeable batteries, fuel cells, and supercapacitors. Among them, lithium ion batteries have successfully become the dominant power sources for portable electronic devices, and their usage has been expanded into larger units such as electric vehicles, robots, *etc*. Group IV elements such as silicon (Si), germanium (Ge) and tin (Sn) are considered to be the most promising alternatives to commercial carbon materials in lithium (Li) ion batteries (LIBs). They are known to have higher theoretical capacities (4200 mA h $g^{-1}$ for Si, 1620 mA h $g^{-1}$ for Ge and 990 mA h $g^{-1}$ for Sn) than graphite carbon (370 mA h $g^{-1}$) owing to a Li-rich alloy formation (i.e., $Li_{4.4}Ge$ and $Li_{4.4}Sn$).[1-3] Ge has attracted increasing attention due to unique merits, such as a 400 times faster $Li^+$ diffusivity than Si, despite a smaller charge capacity than that of Si.[4] However, large volume changes (about 260 % for both Ge and Sn) during lithiation/delithiation induce a pulverization and mechanical stress. This diminishes the electrical interface contact and leads to capacity fading in the bulk electrodes. A large number of papers have shown that the use of oxide forms, such as $GeO_2$ and $SnO_2$, can increase the capacity by forming stable solid electrolyte interphase (SEI) layers that mitigate the volume-change stress.[5-13] Furthermore, it was suggested that the reversible conversion reaction, $GeO_2$ (or $SnO_2$) $+ 4Li^+ + 4e^- \leftrightarrow$ Ge (or Sn) $+ 2Li_2O$, increases the capacities.[6-8,11,12]

$Zn_2GeO_4$ and $Zn_2SnO_4$ have recently attracted a great deal of attention since Zn, Ge, Sn, and their oxide forms are all electrochemically active species for lithiation/delithiation.[14-38] Meanwhile, the theoretical capacity of ZnO is predicted to be as high as 978 mA h $g^{-1}$ for LIB.[39-41] Herein, we investigate the cycling performance of $Zn_2GeO_4$ and $Zn_2SnO_4$ nanowires (NWs) in LIBs. High-purity NWs were synthesized using a hydrothermal method. The use of nanostructures can increase the surface area and reduce the diffusion path length for $Li^+$, so the lithiation/delithiation would proceed more efficiently. Furthermore, the NWs could form a network that releases the volume-change stress. It is thus expected to reduce the degradation of the cycling performance and extend the battery lifetime.

In recent years, sodium ion batteries (SIBs) have gained much interest as an attractive alternative to LIBs because of the natural abundance and low cost of sodium (Na).[42,43] The similarities between $Li^+$ and $Na^+$ intercalation reactions allow the use of analogous materials; instead of the Li ion, the Na ion transfers charges between the anode and the cathode. Therefore, the components of the LIBs can be configured to displace the SIBs. However, the larger size of $Na^+$ (radius = 1.02 Å) as compared to $Li^+$ (radius = 0.59 Å) induces a more significant volume expansion (up to 420 %), which makes it difficult to simply adopt the recent strategies proposed for high-performance LIBs. It was recognized that Ge and Sn accommodate only up to 1 and 3.75 $Na^+$, respectively, which are less than those of LIBs.[44] The theoretical capacity of pure Ge and Sn is thus expected to be 369 and 847 mA h $g^{-1}$, respectively. The higher capacity of Sn has brought more research compared to Ge compounds by utilizing the carbon composites or alloys.[45-55] In this work, we examine the cycling performance of $Zn_2GeO_4$ and $Zn_2SnO_4$ NWs as anode materials in SIBs. To the best of our knowledge, the cycling performance of SIBs has not been reported for these compounds. The comparative studies for LIBs and SIBs would provide a better understanding of the electrochemical reactions that occur at the electrodes.[47,51,55]

[a] Department of Chemistry, Korea University, Jochiwon 339-700, Korea. E-mail: parkjh@korea.ac.kr
[b] Center for Energy Convergence, Korea Institute of Science and Technology, Seoul 136-791, Korea. E-mail: wonic@kist.re.kr
[c] Department of Liberal Art and Literature, Hoseo University, Chungnam 336-795, Korea. E-mail: chaeunhee@hoseo.edu
† Electronic Supplementary Information (ESI) available: XRD data. See DOI: 10.1039/x0xx00000x

## Experimental

The hydrothermal syntheses of $Zn_2GeO_4$ and $Zn_2SnO_4$ NWs are described elsewhere.[56,57] For $Zn_2GeO_4$ NWs, 0.52 g of $GeO_2$ and 1.10 g of $Zn(CH_3COO)_2 \cdot 2H_2O$ were dissolved in 5 mL $H_2O$ and 10 mL ethylenediamine (EDA). To synthesize $Zn_2SnO_4$ NWs, 0.21 g of $SnCl_4 \cdot 5H_2O$ and 0.26 g of $Zn(CH_3COO)_2 \cdot 2H_2O$ were dissolved in a mixture of 15 mL $H_2O$ and 15 mL EDA, and 0.29 g NaOH was then added to the solution. The reaction mixture was transferred to a Teflon-lined stainless-steel autoclave with a 25 mL inner volume. A hydrothermal reaction was performed under an auto-generated pressure at 180-200 °C for 24 h in an electric oven. The product was collected by centrifugation, washed thoroughly with deionized water and ethanol several times, and then dried at 60 °C for 24 h. A white $Zn_2GeO_4$ or $Zn_2SnO_4$ powder was obtained, and then mixed with reduced graphene oxide (RGO) at a weight ratio of 8:2 using sonication. Graphene oxide was synthesized by a modified version of Hummers' method, and reduced using $H_2$ gas at 800 ºC to obtain the reduced form (RGO). Thermogravimetric analysis (TGA) data confirned the ratio of $Zn_2GeO_4$ (or $Zn_2SnO_4$) and RGO, as shown in Fig. S1 (ESI†). Surface area using $N_2$ adsorption-desorption isotherms was measured to be 41.00 and 60.16 $m^2/g$ (see ESI†, Table S1).

The products were characterized by scanning electron microscopy (SEM, Hitachi S-4700), field-emission transmission electron microscopy (FE TEM, FEI TECNAI G2 200 kV and Jeol JEM 2100F), and energy-dispersive X-ray fluorescence spectroscopy (EDX). Fast Fourier-transform (FFT) images were generated by the inversion of the TEM images using Digital Micrograph GMS1.4 software (Gatan Inc.). X-ray diffraction (XRD) pattern measurements were also carried out in a Rigaku D/MAX-2500 V/PC using Cu $K_\alpha$ radiation ($\lambda$ = 1.54056 Å). High-resolution XRD patterns were obtained using the 9B and 3D beamlines of the Pohang Light Source (PLS) with monochromatic radiation ($\lambda$ = 1.54595 Å). TGA was performed using a TA Instruments Ltd. SDT Q600 System. Samples were heated in a flow of $N_2$/air mixture (100 sccm) at 10 ºC/min from room temperature to 1000 ºC. $N_2$ adsorption-desorption isotherms were measured at 77 K on a Micromeritics Tristar 3000 analyzer.

For electrochemical tests, the electrodes of the battery test cells were made of the active material, carbon black (Super P), and polyacrylic acid (PAA, 35 wt% dissolved in water; Aldrich) binder at a weight ratio of 6:2:2. The distilled ethanol-mixed slurry was coated onto the 10 µm-thick Cu foil. The coated electrode was dried at 80 °C for 12 h and then roll-pressed. The thickness of the film was 100 µm. The active materials was on average 0.5 $mg/cm^2$. The coin-type half-cells (CR2032) were prepared in an argon-filled glove box. The LIB cell consisted of an electrode (containing the active material), the Li metal, a micro-porous polyethylene separator, and an electrolyte solution of 1 M $LiPF_6$ in 1:1:1 volume ratio of ethylene carbonate (EC), ethyl methyl carbonate (EMC), and dimethyl carbonate (DMC). Fluoroethylene carbonate (FEC) was used at 5 wt% as an electrolyte additive. The SIB cells consisted of a sample electrode, Na metal, glass fiber separator, and electrolyte solution of 1 M $NaPF_6$ in a 1:1:1 volume ratio of EC, diethyl carbonate (DEC), and DMC, containing 5 wt% FEC additives.

Cyclic voltammetry (CV) measurements were conducted (Biology SAS) in a voltage range of 0.01-3 V at a rate of 0.1 mV $s^{-1}$. The performance of the cells was examined using a battery testing system (Maccor 4000) at a current density of 0.1-5 C between 0.01 and 3 V. We usually fabricated 10 LIB (and SIB) cells for each composition, and took the data that represent the average value. Electrochemical impedance spectroscopy (EIS, Solartron Multistat) measurements were carried out by applying an AC voltage of 5 mV in the frequency range of 100 kHz to 0.01 Hz. For *ex situ* XRD, half-cells charged or discharged to certain voltages were disassembled in a glovebox, and the electrodes were rinsed thoroughly with a DMC solution to remove the $LiPF_6$ or $NaPF_6$ salts.

## Results and discussion

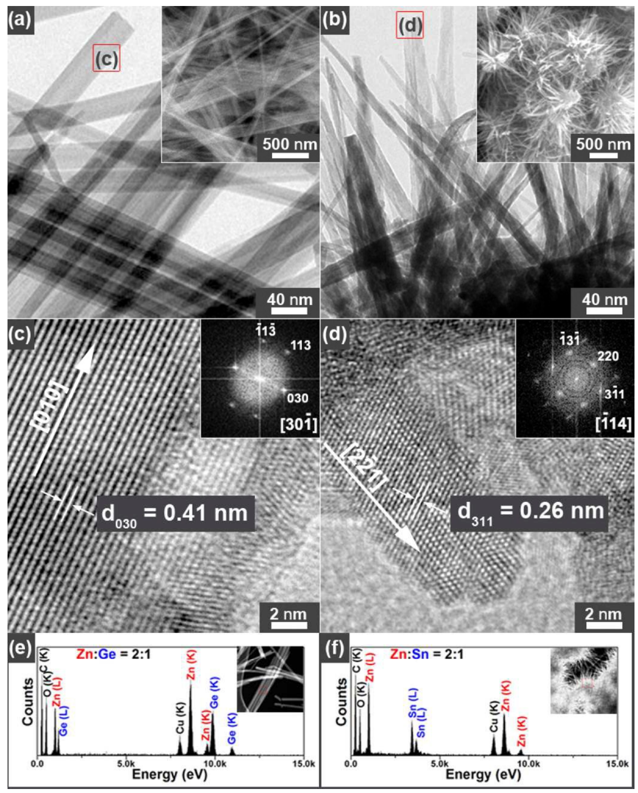


**Fig. 1** SEM and HRTEM images showing the general morphology of (a) $Zn_2GeO_4$ and (b) $Zn_2SnO_4$ NWs. Lattice-resolved images reveal (c) $d_{030}$ = 4.1 Å (at the zone axis of [30$\bar{1}$]) for rhombohedral phase $Zn_2GeO_4$ and (d) $d_{311}$ = 2.6 Å (at the zone axis of [$\bar{1}$14]) for the cubic phase $Zn_2SnO_4$. The EDX spectra (with HAADF STEM images in the insets) show the composition of the (e) $Zn_2GeO_4$ and (f) $Zn_2SnO_4$ NWs.

XRD patterns for $Zn_2GeO_4$ and $Zn_2SnO_4$ NWs are shown in Fig. S2 (ESI†). All peaks were well matched with those of the references, rhombohedral phase $Zn_2GeO_4$ (JCPDS No. 11-0687; $a$ = 14.23 Å, $c$ = 9.530 Å) and cubic phase $Zn_2SnO_4$ (JCPDS No. 24-1470; $a$ = 8.657 Å), confirming the high purity of the samples. Figs. 1a and 1b show SEM and high-resolution TEM (HRTEM) images of the $Zn_2GeO_4$ and $Zn_2SnO_4$ NWs, respectively. The $Zn_2GeO_4$ NWs have a homogeneous diameter distribution with an average of 50 nm. The $Zn_2SnO_4$ NWs usually have sea urchin-like morphologies with diameters of 20-40 nm. Fig. 1c shows the lattice-resolved image of the $Zn_2GeO_4$ NW and the corresponding FFT image at the [30$\bar{1}$] zone axis. The growth direction is uniformly [010]. The $d$-spacing of the

(030) planes is about 4.1 Å, which is consistent with that of the rhombohedral phase $Zn_2GeO_4$. The lattice-resolved image of the $Zn_2SnO_4$ NWs and the corresponding FFT image at the [$\bar{1}$14] zone axis show that the growth direction is [112] (Fig. 1d). The *d*-spacing of the (311) planes is about 2.6 Å, corresponding to the cubic phase $Zn_2SnO_4$. Figs. 1e and 1f show high-angle annular dark field (HAADF) scanning TEM (STEM) images and EDX spectra of $Zn_2GeO_4$ and $Zn_2SnO_4$ NWs, respectively, confirming that the composition ratio of Zn and Ge (or Sn) was 2:1. TEM images for the mixture of NW-graphene are shown in Fig. S3 (ESI†).

The electrochemical properties of $Zn_2GeO_4$ and $Zn_2SnO_4$ acting as anode materials in LIBs were examined. The results are summarized in Tables 1 and 2. For convenience, we define the discharge–charge rate (current rate, C rate) using the theoretical capacity; 1 C = 641 mA g$^{-1}$ for $Zn_2GeO_4$ and 1 C = 547 mA g$^{-1}$ for $Zn_2SnO_4$. The basis of the calculation will be explained later using the reaction mechanism.

CV curves of LIBs revealed several reduction-oxidation (redox) peak pairs (Figs. 2a and 2b). The scan rate is 0.05 mVs$^{-1}$ for the 1$^{st}$ and 2$^{nd}$ cycles, and 0.1 mVs$^{-1}$ for the 3$^{rd}$ and 10$^{th}$ cycles. $Zn_2GeO_4$ exhibited a cathodic (lithiation) peak at 0.7 V in the first and 0.8-0.9 V in the second/third potential sweeps. This peak was assigned to the decomposition of $Zn_2GeO_4$: $Zn_2GeO_4 + 8Li^+ + 8e^- \rightarrow 2Zn + Ge + 4Li_2O$, and the formation of a SEI. We observed that as the scan rate increases, the cathodic peak of the 1$^{st}$ cycle shifts to the lower voltage, as shown in Fig. S4 (ESI†). It indicates that the decomposition of $Zn_2GeO_4$ is kinetically unfavorable. After the formation of SEI in the 1$^{st}$ cycle, the decomposition becomes active at 0.8-0.9 V.

An anodic peak at 1.3 V was attributed to the oxidation reaction of Zn and Ge with $Li_2O$. The signature of the reversible Li-alloying reaction of Zn and Ge appeared as a pair of peaks at potentials of around 0.02 V and 0.3 V. At the 10$^{th}$ cycle, while the catodic peak at 0.8-0.9 V disappears, there exists redox pair peaks at around 0.5 V and 1.3 V, suggesting a possibility for the reversible conversion reaction: $ZnO + 2Li^+ + 2e^- \leftrightarrow Zn + Li_2O$ and $GeO_2 + 4Li^+ + 4e^- \leftrightarrow Ge + 2Li_2O$.

For $Zn_2SnO_4$, a cathodic peak at 0.6 V in the first potential sweep was due to the decomposition of $Zn_2SnO_4$: $Zn_2SnO_4 + 8Li^+ + 8e^- \rightarrow 2Zn + Sn + 4Li_2O$. The formation of the SEI layer could result in the stronger cathodic peak. A pair of redox peaks at potentials of around 0.02 V and 0.3 V was ascribed to the reversible alloying reaction of Zn and Sn. After the 1$^{st}$ cycle, the cathodic peak at 0.5 V and the anodic peak at 1.3 V were observed, providing definite evidence for the reversible conversion reaction of Zn and Sn: $ZnO + 2Li^+ + 2e^- \leftrightarrow Zn + Li_2O$ and $GeO_2 + 4Li^+ + 4e^- \leftrightarrow Ge + 2Li_2O$. The cathodic peak at 0.8-0.9 V consistently appears, probably due to the residual $Zn_2SnO_4$ phase. Similarly to the case of $Zn_2GeO_4$, the cathodic peak of the 1$^{st}$ cycle shifts to the lower voltage, due to the kinetically unfavorable decomposition of $Zn_2SnO_4$ (see Fig. S4, ESI†). After the 1$^{st}$ cycle, the decomposition occurs more efficiently at 0.8-0.9 V.

Figs. 2c and 2d show the voltage profiles (current-voltage or I-V data) of coin-type half-cells prepared using $Zn_2GeO_4$ and $Zn_2SnO_4$ NWs for 1, 5, 10, 50, and 100 cycles at a rate of 0.1 C, tested between 0.01 and 3.0 V, respectively. On the basis of the half-cell reaction in this study, the insertion of $Li^+$ into the NW electrode is referred to as discharge, and the extraction of $Li^+$ from the electrode is referred to as charge. There was a plateau at approximately 0.8 V and 0.9 V in the first discharge curve of $Zn_2GeO_4$ and $Zn_2SnO_4$, respectively, due to the decomposition reaction. The discharge curves of $Zn_2GeO_4$ and $Zn_2SnO_4$ showed a plateau region at approximately 0.2 V in all cycles, due to the alloying reaction. After the first cycle, the plateau appeared constantly at around 0.5 V, respectively, which is ascribed to the reversible conversion reaction.

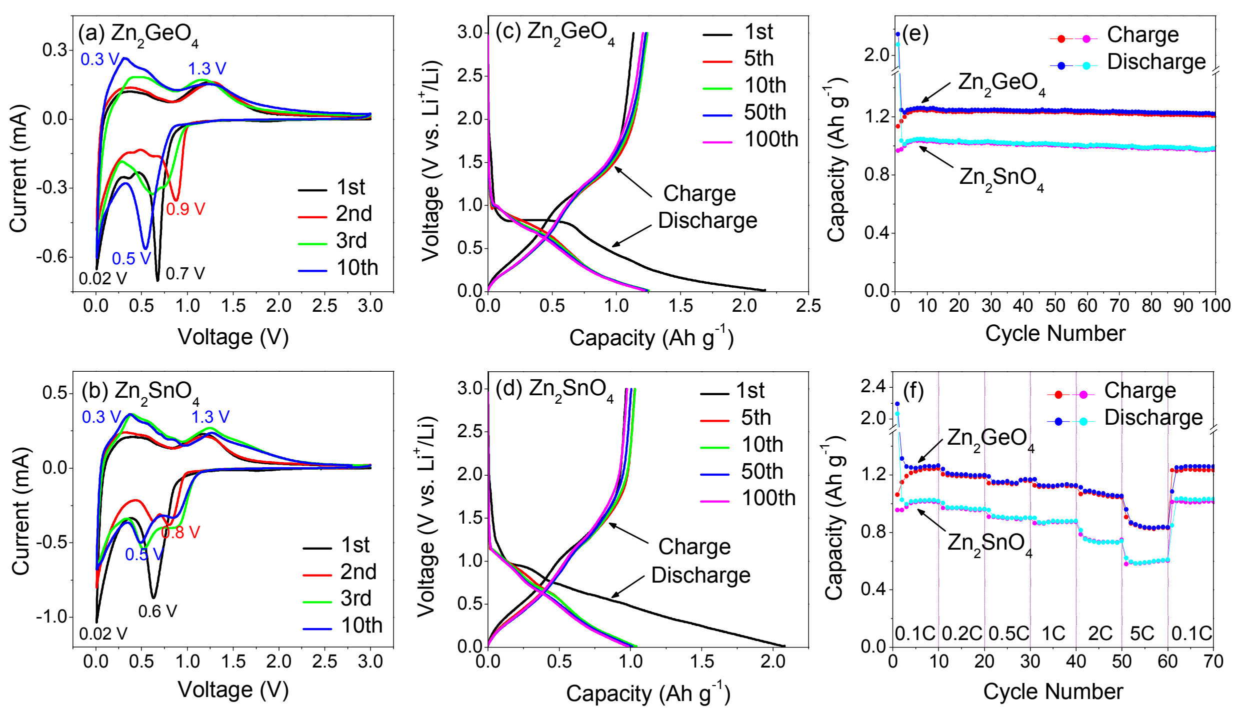


**Fig. 2** Cyclic voltammetry curves of (a) $Zn_2GeO_4$ and (b) $Zn_2SnO_4$ for the first 10 cycles of LIBs. Charge and discharge voltage profiles of

LIB half-cell using (c) $Zn_2GeO_4$ and (d) $Zn_2SnO_4$ for 1, 5, 10, 50, and 100 cycles tested between 0.01 and 3 V, at a rate of 0.1 C. (e) Charge/discharge capacity vs. cycle number for half cells of $Zn_2GeO_4$ and $Zn_2SnO_4$. (f) Cycling performance of $Zn_2GeO_4$ and $Zn_2SnO_4$ as the rate is increased from 0.1 C to 5 C.

**Table 1**. Summary of the LIB and SIB half-cell capacities (mA h $g^{-1}$) of $Zn_2GeO_4$ and $Zn_2SnO_4$ during the cycles at a rate of 0.1 C.

| | | Theoretical capacity | | First cycle | | | $5^{th}$ cycle | $50^{th}$ cycle | $100^{th}$ cycle | |
|---|---|---|---|---|---|---|---|---|---|---|
| | | A[a] | B[b] | discharge | charge | η (%)[c] | discharge | discharge | discharge | η (%)[d] |
| LIB | $Zn_2GeO_4$ | 641 | 1443 | 2161 | 1135 | 52.5 | 1250 | 1241 | 1220 | 99.1 |
| | $Zn_2SnO_4$ | 547 | 1231 | 2081 | 969 | 46.5 | 1037 | 1012 | 983 | 99.3 |
| SIB | $Zn_2GeO_4$ | 100 | 902 | 912 | 442 | 48.4 | 435 | 354 | 342 | 99.3 |
| | $Zn_2SnO_4$ | 320 | 1004 | 851 | 446 | 52.5 | 421 | 328 | 306 | 98.9 |

[a] Calculated using 6.4 Li intercalation based on mechanism "A" (see text); [b] Calculated using 14.4 Li intercalation based on mechanism "B" (see text); [c] Coulombic efficiency for the first cycles. [d] Coulombic efficiency for 5-100 cycles

**Table 2**. Summary of the LIB and SIB half-cell (discharge) capacities (mA h $g^{-1}$) of $Zn_2GeO_4$ and $Zn_2SnO_4$ as the rate was increased from 0.1 C to 5 C.

| | | 0.1 C | 0.2 C | 0.5 C | 1 C | 2 C | 5 C | 0.1 C |
|---|---|---|---|---|---|---|---|---|
| | | $5^{th}$ | $15^{th}$ | $25^{th}$ | $35^{th}$ | $45^{th}$ | $55^{th}$ | $65^{th}$ |
| LIB | $Zn_2GeO_4$ | 1247 | 1201 | 1154 | 1123 | 1074 | 834 | 1259 |
| | $Zn_2SnO_4$ | 1018 | 972 | 899 | 879 | 730 | 591 | 1027 |
| SIB | $Zn_2GeO_4$ | 369 | 316 | 301 | 295 | 278 | 256 | 348 |
| | $Zn_2SnO_4$ | 381 | 335 | 294 | 264 | 238 | 201 | 340 |

Fig. 2e shows the discharge-charge capacities of $Zn_2GeO_4$ and $Zn_2SnO_4$ NWs as a function of the cycle number up to 100 cycles. The first discharge and charge capacities of $Zn_2GeO_4$ were 2161 and 1135 mA h $g^{-1}$, respectively, with a coulombic efficiency of 52.5 %. In the case of $Zn_2SnO_4$, they were 2081 and 969 mA h $g^{-1}$, respectively, with a coulombic efficiency of 46.5 %. The discharge capacities after 100 cycles were 1220 and 983 mA h $g^{-1}$, respectively, for $Zn_2GeO_4$ and $Zn_2SnO_4$ NWs. The coulombic efficiency vs. cycle number is plotted in Fig. S5 (ESI†). After the first cycle, they exhibited excellent capacity reversibility; the respective average coulombic efficiencies were 99.1 and 99.3 % for 5-100 cycles.

We summarized the previous works on $Zn_2GeO_4$ and $ZnSn_2O_4$ nanostructures as LIB anodes, reported by other research groups, as shown in Tables S2 and S3 (ESI†). Our capacity value for $Zn_2GeO_4$ NWs is comparable to the best results: 1300 mA h $g^{-1}$ after 140 cycles for $Zn_2GeO_4$@g-$C_3N_4$ nanoparticle@nanosheet composites that reported by X. Li *et al.*;[21] 1301 mA h $g^{-1}$ after 100 cycles for Mn-doped $Zn_2GeO_4$ nanosheets that reported by Q. Li *et al.*[23] The capacity of the present $Zn_2SnO_4$ NWs is larger than that of $Zn_2SnO_4$ powders: 856 mA h $g^{-1}$ after 50 cycles reported by Lee and Lee.[27]

The rate capability and the retention ability were evaluated by increasing the C rate step-wise from 0.1 C to 5 C, and then returning back to 0.1 C. Fig. 2f displays the discharge–charge capacities as the C rate changes by steps of 0.1 C→0.2 C→0.5 C→1 C→2 C→5 C→0.1 C (total of 70 cycles). For each C rate, 10 cycles were performed. As the C rate reached 5 C, the discharge capacity decreased to 834 and 591 mA h $g^{-1}$ (at the $55^{th}$ cycle), for $Zn_2GeO_4$ and $Zn_2SnO_4$, respectively (see Table 2). When the C rate returned to 0.1 C, the capacity turned to 1259 and 1027 mA h $g^{-1}$ (at the $65^{th}$ cycle) from 1247 and 1018 mA h $g^{-1}$ (at the $5^{th}$ cycle), respectively; the recovery was about 100 %.

*Ex situ* XRD patterns of the $Zn_2GeO_4$ and $Zn_2SnO_4$ NW electrodes (discharged/charged) were measured, as shown in Fig. S6 (ESI†). After the first discharge, all of the $Zn_2GeO_4$ and $Zn_2SnO_4$ had completely decomposed. For $Zn_2GeO_4$, no Zn (or ZnO) or Ge peaks were detected, indicating complete amorphization upon discharge. In contrast, $Zn_2SnO_4$ showed the formation of tetragonal phase Sn (β-Sn). As the number of cycles increased up to 20 cycles, cubic phase Sn (α-Sn) became a dominant phase. We observed the same phase evolution for Sn, $SnO_2$, and $SnS_2$.[58] First-principles calculations of the Li intercalation energy of α-Sn and β-Sn predicted that the lithiated form of α-Sn is thermodynamically more stable than that of β-Sn, thereby β-Sn can be converted to the more stable α-Sn upon lithiation. HRTEM images of the $Zn_2GeO_4$ and $Zn_2SnO_4$ NW electrodes (discharged/charged) were measured to confirm those phase evolution, as shown in Figs. S7 and S8 (ESI†).

The electrochemical reactions for $Zn_2GeO_4$ and $Zn_2SnO_4$ are equated as follows:

For $Zn_2GeO_4$,

(1) $Zn_2GeO_4 + 8Li^+ + 8e^- \rightarrow 2Zn + Ge + 4Li_2O$

(2) $2Zn + 2xLi^+ + 2xe^- \leftrightarrow 2Li_xZn$ ($x \leq 1$)

(3) $Ge + yLi^+ + ye^- \leftrightarrow Li_yGe$ ($y \leq 4.4$)

(4) $2ZnO + 4Li^+ + 4e^- \leftrightarrow 2Zn + 2Li_2O$

(5) $GeO_2 + 4Li^+ + 4e^- \leftrightarrow Ge + 2Li_2O$

For $Zn_2SnO_4$,

(6) $Zn_2SnO_4 + 8Li^+ + 8e^- \rightarrow 2Zn + Sn + 4Li_2O$

(7) $2Zn + 2xLi^+ + 2xe^- \leftrightarrow 2Li_xZn$ ($x \leq 1$)

(8) $Sn + yLi^+ + ye^- \leftrightarrow Li_ySn$ ($y \leq 4.4$)

(9) $2ZnO + 4Li^+ + 4e^- \leftrightarrow 2Zn + 2Li_2O$

(10) $SnO_2 + 4Li^+ + 4e^- \leftrightarrow Sn + 2Li_2O$

Steps (1) and (6) correspond to the decomposition reaction of $Zn_2GeO_4$ and $Zn_2SnO_4$, respectively. Steps (2)/(3) (or (7)/(8)) represent the reversible alloying reaction of Zn and Ge (or Sn) with Li. We assumed that Zn formed LiZn ($x$ = 1) and Ge (or Sn) formed $y$ = 4.4 alloys, $Li_{22}Ge_5$ (or $Li_{22}Sn_5$). If the first discharge reaction induced all (1)-(3) (or (6)-(8)) reactions in forward direction, a total of 14.4 Li ions participated in the intercalation and produced the capacity, 14.4 × 26800/M mA h $g^{-1}$, where M is the molecular weight for $Zn_2GeO_4$ (267.39 g $mol^{-1}$) and $Zn_2SnO_4$ (313.49 g $mol^{-1}$). Then, the theoretical capacity would be expected to be 1443 and 1231 mA h $g^{-1}$ for $Zn_2GeO_4$ and $Zn_2SnO_4$, respectively. The first discharge gave capacities of 2161 and 2081 mA h $g^{-1}$, respectively, which are higher than the theoretical capacities. It could be attributed to the increased active surface area of the smaller size nanocrystals compared to that of the bulk. If reversible alloying reactions (2)/(3) or (7)/(8) occurred predominantly after the first cycle (referred to as mechanism "A"), then the theoretical capacities are calculated as 641 mA h $g^{-1}$ for $Zn_2GeO_4$ and 547 mA h $g^{-1}$ for $Zn_2SnO_4$, due to the total 6.4 Li intercalation. We defined the C rate using these values.

The discharge capacity of $Zn_2GeO_4$ after 100 cycles was remarkably 1220 mA h $g^{-1}$, which is much higher than the theoretical capacity of mechanism "A". Therefore, the addition of reversible conversion reactions (4) and (5) increased the capacities, which was strongly supported by the CV and I-V data. We referred to this mechanism as "B". $GeO_2$ and ZnO are presumably amorphous phase (e.g., $GeO_x$ with $x < 2$). Our capacity value is lower than the theoretical value (1443 mA h $g^{-1}$), probably due to the amorphous oxide phase. Many previous works also reported the contribution of these conversion reactions, which is essentially the same as our model.[15-23]

The discharge capacity of $Zn_2SnO_4$ after 100 cycles (983 mA h $g^{-1}$) is larger than the theoretical capacity (547 mA h $g^{-1}$) of mechanism "A". Based on the CV and I-V data, we proposed the contribution of the reversible conversion reactions (9) and (10). We referred to as mechanism "B". A number of research groups also suggested the partial contribution of these reactions.[30,34,36-38] Our value is less than the theoretical capacity (1231 mA h $g^{-1}$) of mechanism "B". The remaining portion of the crystalline α- and β-Sn phase could be evidence for an incomplete alloying reaction. Our group calculated a lower stability of the lithiated alloy for α-Sn compared to that of β-Sn.[58] It means that α-Sn has not lithiated, which plays a crucial role in reducing the capacities.

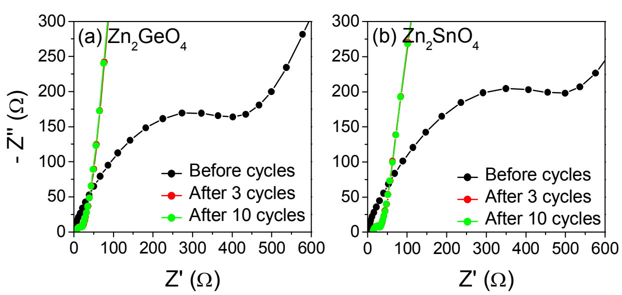


**Fig. 3** Nyquist plots of (c) $Zn_2GeO_4$ and (d) $Zn_2SnO_4$ for the first 10 cycles in LIBs.

Fig. 3 shows the Nyquist plots of the EIS measurement results before the cycling test and after 3rd and 10th cycles. Z′ and Z″ correspond to the real and imaginary components of impedence. Before the cycling test, the plots consist of one semicircle in the high frequency region and a straight line in the low frequency region. The semicircle portion is related to the reaction at the active materials/electrolyte interface and reflects the charge transfer impedances. Therefore, the diameter of the semicircle is attributed to the charge transfer resistance ($R_{ct}$). The $Zn_2GeO_4$ electrode had a smaller diameter than the $Zn_2SnO_4$ electrode, indicating a lower charge transfer resistance in the $Zn_2GeO_4$ electrode. The $R_{ct}$ values of $Zn_2GeO_4$ and $Zn_2SnO_4$ were estimated to be 440 and 525 Ω, respectively, using curve fit analysis (see Table S4 in ESI†). This explains why $Zn_2GeO_4$ exhibited higher initial capacities than $Zn_2SnO_4$.

After the first cycle, the shape of the impedance spectrum changed and the semicircle sizes dramatically decreased compared to those observed in the initial cells. Since the phase change from $Zn_2GeO_4$ (or $Zn_2SnO_4$) to Zn, Ge (or Sn), and oxide form occurred after the first cycle, the observed impedance spectra may correspond to the $R_{ct}$ that is related to the products, and the resistance ($R_{SEI}$) of the SEI layers between the electrode and the electrolyte. $R_{ct}$ is 10 and 13 Ω (after 10th cycles), respectively, for $Zn_2GeO_4$ and $Zn_2SnO_4$. The electrical conductivity of Zn and Ge (or Sn) was expected to be much higher than that of $Zn_2GeO_4$ (or $Zn_2SnO_4$), which could be associated to these lower $R_{ct}$ values. The $R_{SEI}$ value of $Zn_2GeO_4$ and $Zn_2SnO_4$ was estimated to be 3 Ω. The results are well correlated with the capacities of $Zn_2GeO_4$ and $Zn_2SnO_4$.

As next step, the electrochemical properties of $Zn_2GeO_4$ and $Zn_2SnO_4$ NW acting as anode materials in SIBs were studied, and the results are summarized in Table 1 and Table 2. We defined the 1 C rate as 100 and 320 mA $g^{-1}$ for $Zn_2GeO_4$ and $Zn_2SnO_4$, respectively. The calculation of these values will be explained using the reaction mechanism.

The CV curve of $Zn_2GeO_4$ shows a cathodic peak at around 0.3 V in the first potential sweep, which was attributed to the decomposition of $Zn_2GeO_4$ (Fig. 4a). The signature of the Na-Ge alloying reaction appeared as a pair of redox peaks at potentials of around 0.01 V and 0.2 V, respectively. There were another redox peaks at 0.3 V and 0.95 V, whose intensity increases after the first cycle. Based on the LIB data, we suggest that these peaks are ascribed to the reversible conversion reactions such as $ZnO + 2Na^+ + 2e^- \leftrightarrow Zn + Na_2O$ and $GeO_2 + 4Na^+ + 4e^- \leftrightarrow Ge + 2Na_2O$. Fig. 4b corresponds to the CV curves of $Zn_2SnO_4$. A cathodic peak at 0.7 V in the first potential sweep was assigned to the decomposition of $Zn_2SnO_4$. A pair of redox peaks at potentials of around 0.01 V and 0.3 V must originate from the reversible Na-Sn alloying reaction. After the first cycle, the redox peaks at around 0.2 V and 0.9 V constantly appeared, which suggests a possibility that the conversion reactions ($ZnO + 2Na^+ + 2e^- \leftrightarrow Zn + Na_2O$ and $SnO_2 + 4Na^+ + 4e^- \leftrightarrow Sn + 2Na_2O$) proceeded reversibly upon cycling.

Figs. 4c and 4d show the voltage profiles of coin-type half-cells prepared using $Zn_2GeO_4$ and $Zn_2SnO_4$ for 1, 5, 10, 50, and 100 cycles, at a rate of 0.1 C (= 10 and 32 mA $g^{-1}$, respectively), tested between 0.01 and 3.0 V. The first discharge and charge capacities of $Zn_2GeO_4$ were 912 and 442 mA h $g^{-1}$, respectively, with a coulombic efficiency of 48.4 %. The first discharge and charge capacities of $Zn_2SnO_4$ were 851 and 446 mA h $g^{-1}$, respectively, with a coulombic efficiency of 52.5 %. The discharge curves showed a plateau region at approximately 0.1 V in all cycles, due to the Na alloying reactions of Ge or Sn. $Zn_2GeO_4$ exhibited another plateau at approximately 0.4 V in all discharge processes, which could be due to the reversible conversion reaction. For $Zn_2SnO_4$, this plateau appeared in a shorter region at around 0.3 V compared to that of $Zn_2GeO_4$.

Fig. 4e shows the discharge–charge capacities of $Zn_2GeO_4$ and $Zn_2SnO_4$ as a function of the cycle number up to 100. After the first cycle, their capacities exhibited excellent reversibility. The discharge capacities for 100th cycles were 342 and 306 mA h $g^{-1}$, respectively, for $Zn_2GeO_4$ and $Zn_2SnO_4$. The coulombic efficiency vs. cycle number is plotted in Fig. S2. The respective average coulombic efficiency was 99.3 and 98.9 % for 5-100 cycles. Both $Zn_2GeO_4$ and $Zn_2SnO_4$ showed excellent cyclability.

The rate capability was monitored by increasing the C rate step-wise from 0.1 C to 5 C, and then returning back to 0.1 C. Fig. 4f displays the discharge-charge capacities as the C rate changes by steps of 0.1 C→0.2 C→0.5 C→1 C→2 C→5 C→0.1 C. For each C rate, 10 cycles were performed. The initial respective discharge capacities (0.1 C) at the 5th cycle were 369 and 381 mA h $g^{-1}$, respectively. As the C rate reached 5 C, the capacities decreased to 256 and 201 mA h $g^{-1}$ (at the 55th cycle) for $Zn_2GeO_4$ and $Zn_2SnO_4$, respectively (see Table 2). When the C rate was returned back to 0.1 C, the capacity increased to 348 and 340 mA h $g^{-1}$ (at the 65th cycle), respectively, showing an excellent retention ability (94 and 89 %).

The electrochemical reactions for the sothiation/desothiation of $Zn_2GeO_4$ are described as follows:

(11) $Zn_2GeO_4 + 8Na^+ + 8e^- \rightarrow 2Zn + Ge + 4Na_2O$
(12) $Ge + xNa^+ + xe^- \leftrightarrow Na_xGe$ ($x \leq 1$)
(13) $2ZnO + 4Na^+ + 4e^- \leftrightarrow 2Zn + 2Na_2O$
(14) $GeO_2 + 4Na^+ + 4e^- \leftrightarrow Ge + 2Na_2O$

Step (11) corresponds to the decomposition reaction upon sothiation. We assumed that Ge formed a 1:1 Na:Ge alloy for reversible alloying reaction (12). If the first discharge induced reaction (11) and forward reaction (12), the total 9 Na ion intercalation produced a theoretical capacity of 902 mA h $g^{-1}$. The first discharge had a capacity of 912 mA h $g^{-1}$, which is close to the theoretical value. If only reaction (12) occurred reversibly after the first cycle, the theoretical capacity is expected to be 100 mA h $g^{-1}$. We define the C rate based on this mechanism (referred to as mechanism "A"). However, our discharge capacity after 100 cycles was 342 mA h $g^{-1}$, which is much larger than the theoretical value. Therefore the conversion reactions (13) and (14) may contribute partially in the reversible reaction, which is similar to the case for the LIB. We refer to this as mechanism "B". The higher capacity of the Ge nanostructures than the theoretical capacity in SIBs was also reported and attributed to the faster diffusion of Na ions at the surface.[46,47] We suggest that the amorphous Ge or $GeO_x$ could have a faster diffusion rate of $Na^+$ than the crystalline phase and proceed efficiently the alloy and conversion reactions.

For $Zn_2SnO_4$, the SIB electrochemical reactions are given by two steps:

(15) $Zn_2SnO_4 + 8Na^+ + 8e^- \rightarrow 2Zn + Sn + 4Na_2O$
(16) $Sn + xNa^+ + xe^- \leftrightarrow Na_xGe$ ($x \leq 3.75$)
(17) $2ZnO + 4Na^+ + 4e^- \leftrightarrow 2Zn + 2Na_2O$
(18) $SnO_2 + 4Na^+ + 4e^- \leftrightarrow Sn + 2Na_2O$

It was assumed that Sn bind 3.75 Na in alloying reaction (16). If the first discharge reaction of $Zn_2SnO_4$ contained reactions (15) and (16), the total 11.75 Na intercalation produced the theoretical capacity of 1004 mA h $g^{-1}$. The first discharge showed a capacity of 851 mA h $g^{-1}$, which is less than the theoretical value. If reversible alloying reaction (16) occurred predominantly after the first cycle (referred to as mechanism "A"), the theoretical capacity was expected to be 320 mA h $g^{-1}$, which is about the same as the capacity after the 100th cycle (306 mA h $g^{-1}$).

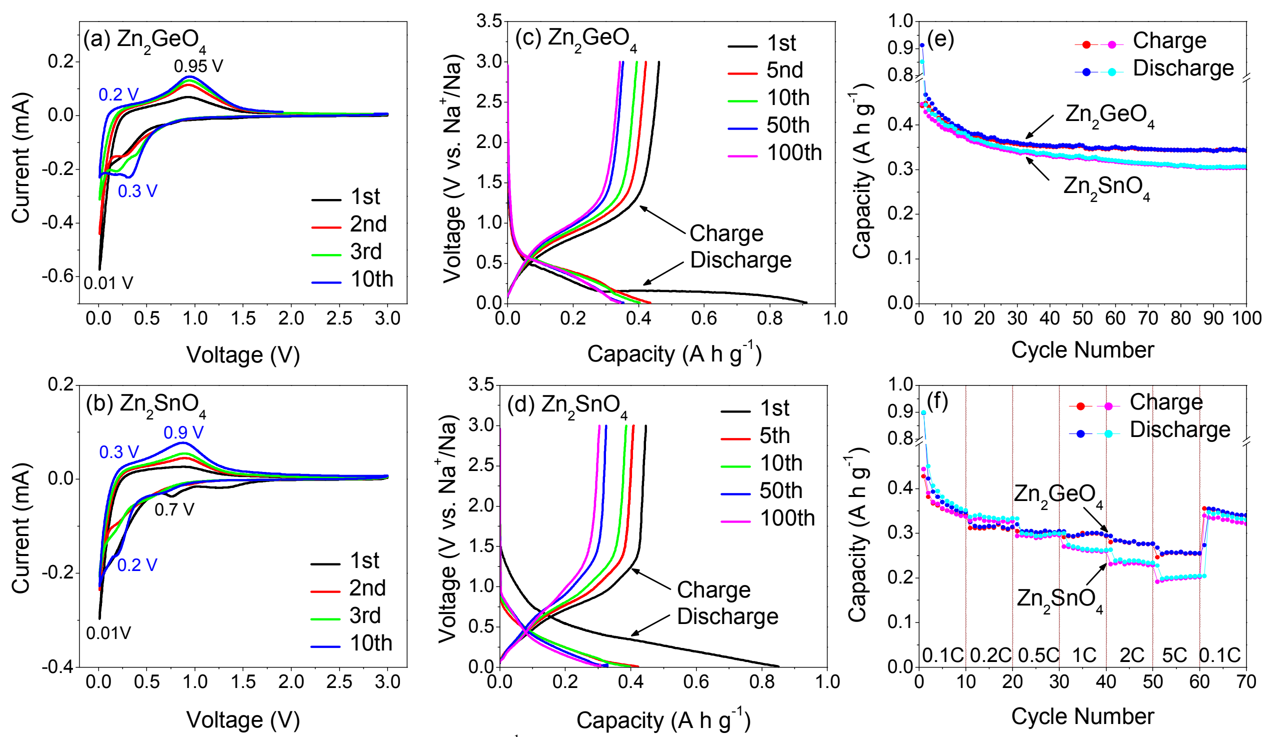


**Fig. 4** Cyclic voltammetry curve (scan rate = 0.1 mV $s^{-1}$) of (a) $Zn_2GeO_4$ and (b) $Zn_2SnO_4$ for the first 10 cycles for the SIB. Charge and discharge voltage profiles of the SIB half-cell using (c) $Zn_2GeO_4$ and (d) $Zn_2SnO_4$ for 1, 5, 10, 50, and 100 cycles tested between 0.01 and 3 V, at a rate of 0.1 C. (e) Charge/discharge capacity vs. cycle number for the half-cells of $Zn_2GeO_4$ and $Zn_2SnO_4$. (f) Cycling performance of $Zn_2GeO_4$ and $Zn_2SnO_4$ as the rate was increased from 0.1 C to 5 C.

*Ex situ* XRD patterns of the $Zn_2GeO_4$ and $Zn_2SnO_4$ SIB electrodes (discharged/charged) were measured as shown in Fig. S9 (ESI†). $Zn_2GeO_4$ completely decomposed into an amorphous phase after the first discharge, while $Zn_2SnO_4$ remained up to the 70$^{th}$ cycle. The production of the β-Sn phase was observed upon cycling. The finding of the $Zn_2SnO_4$ phase as well as the low discharge capacity of the first cycle could be a strong evidence for the incomplete alloy reaction, which is similar to the case of the LIBs. The reduced capacity due to a kinetic difficulty to reach the $Na_{3.75}Sn$ alloy was consistently suggested by the previous works on Sn and $SnO_2$.[52,35] Our CV and I-V data showed a possibility for the reversible conversion reactions (17) and (18) (referred to as mechanism "B"). Therefore, the reversible conversion reaction would contribute in restoring the capacities.

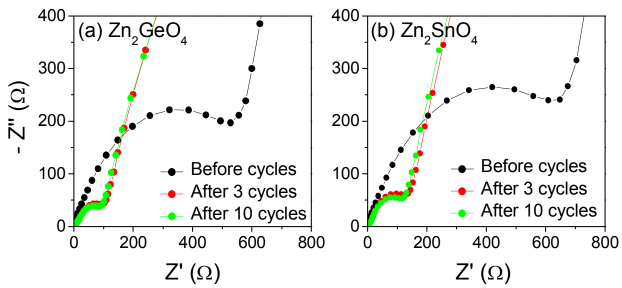


**Fig. 5** Nyquist plots of (c) $Zn_2GeO_4$ and (d) $Zn_2SnO_4$ for the first 10 cycles in SIBs.

Fig. 5 shows the Nyquist plots for $Zn_2GeO_4$ and $Zn_2SnO_4$ before the cycling test and after 3 and 10 cycles in SIBs. In the initial cells, $Zn_2GeO_4$ showed a lower $R_{ct}$ value than $Zn_2SnO_4$; 600 and 720 Ω were obtained by the curve fit analysis (see Table S4 in ESI†). These values are consistent with their initial capacities. The semicircle sizes dramatically decreased after the first cycle. The fitting gives $R_{ct}$ = 83 and 105 Ω (after 10 cycles), respectively, for $Zn_2GeO_4$ and $Zn_2SnO_4$. The $R_{SEI}$ value of $Zn_2GeO_4$ and $Zn_2SnO_4$ was estimated to be about 10 and 13 Ω, respectively, which is well correlated with their capacities. The resistance of the SIB cells was larger that of the LIB cells. In order to decrease the resistance (increase the capacities), the activation of the unreactive materials would be necessary.

## Conclusions

We synthesized high-purity $Zn_2GeO_4$ and $Zn_2SnO_4$ NWs via a hydrothermal method. They consisted of a single-crystalline rhombohedral and cubic phase, respectively. The respective average diameter was 50 and 30 nm. We investigated the electrochemical properties of these $Zn_2GeO_4$ and $Zn_2SnO_4$ NWs as anode materials for LIBs and SIBs. Both $Zn_2GeO_4$ and $Zn_2SnO_4$ showed excellent cycling performance of LIBs; the reversible capacities were 1220 and 983 mA h g$^{-1}$ (at 0.1 C) after 100 cycles, respectively, with a high coulomb efficiency of 99%. We investigated the contribution of the alloy formation reaction of Zn, Ge, and Sn with Li, and the conversion reaction ($ZnO + 2Li^+ + 2e^- \leftrightarrow Zn + Li_2O$ and $GeO_2$ (or $SnO_2$) $+ 4Li^+ + 4e^- \leftrightarrow$ Ge (or Sn) $+ 2Li_2O$) in the capacities. For both $Zn_2GeO_4$ and $Zn_2SnO_4$, the reversible conversion reaction increased the capacities. The persistence of the crystalline Sn phase (*Ex situ* XRD) indicates a kinetic difficulty for the Li–Sn alloying reaction.

In SIBs, the reversible capacities of $Zn_2GeO_4$ and $Zn_2SnO_4$ were 342 and 306 mA h g$^{-1}$ (at 0.1 C) after 100 cycles, respectively, with a high coulomb efficiency of about 99 %. $Zn_2GeO_4$ exhibited a higher capacity than the theoretical capacity (100 mA h g$^{-1}$). The capacity of $Zn_2SnO_4$ is close to the theoretical capacity (320 mA h g$^{-1}$). *Ex situ* XRD data indicate the kinetic difficulty of the Na–Sn alloying reaction. We suggest that the reversible conversion reaction increased the capacities for both $Zn_2GeO_4$ and $Zn_2SnO_4$, which is similar to the case of LIBs. The comparative studies provide a better understanding for sodiation of $Zn_2GeO_4$ and $Zn_2SnO_4$. Finally, the present studies showed that $Zn_2GeO_4$ and $Zn_2SnO_4$ NWs are promising candidates for applications in high-performance LIBs and SIBs.

## Acknowledgements

This study was supported by NRF (20110020090; 2014-R1A1A-2039084; 2009-0082580) and the KIST Institutional Program (2E26291). The HVEM (Daejeon) and XPS (Pusan) measurements were performed at the KBSI. The experiments at the PLS were partially supported by MOST and POSTECH.

## Notes and references

1 M. R. St. John, A. J. Furgala and A. F. Sammells, *J. Electrochem. Soc.,*1982, **129**, 246.
2 J. Graetz, C. C. Ahn, R. Yazami and B. Fultz, *J. Electrochem. Soc.,* 2004, **151**, A698.
3 R. A. Huggins, *J. Power Sources,*1999, **81-82**, 13.
4 M. Winter and J. O. Besenhard, *Electrochim Acta,*1999, **45**, 31.
5 S. Jin, N. Li, H. Cui and C. Wang, *Nano Energy*, 2013, **2**, 1128.
6 K. H. Seng, M. Park, Z. P. Guo, H K. Liu and J. Cho, *Nano Lett.*, 2013, **13**, 1230.
7 D. Lv, M. L. Gordin, R. Yi, T. Xu, J. Song, Y. –B. Jiang, D. Choi and D. Wang, *Adv. Funct. Mater.*, 2014, **24**, 1059.
8 J. Hwang, C. Jo, M. G. Kim, J. Chun, E. Lim, S. Kim, S. Jeong, Y. Kim and J. Lee, *ACS Nano*, 2015, **9**, 5299.
9 Y. Idota, T. Kubota, A. Matsufuji, Y. Maekawa and T. Miyasaka, *Science* 1997, **276**, 1395.
10 S. J. R. Prabakar, Y. –H. Hwang, E. –G. Bae, S. Shim, D. Kim, M. S. Lah, K. –S. Sohn and M. Pyo, *Adv. Mater.*, 2013, **25**, 3307.
11 D. Wang, J. Yang, X. Li, D. Geng, R. Li, M. Cai, T. –K. Sham and X. Sun, *Energy Environ. Sci.*, 2013, **6**, 2900.
12 K. Kisu, M. Iijima, E. Iwama, M. Saito, Y. Orikasa, W. Naoi and K. Naoi, *J. Mater. Chem. A,* 2014, **2**, 13058.
13 J. Sun, L. Xiao, S. Jiang, G. Li, Y. Huang and J. Geng, *Chem. Mater.*, 2015, **27**, 4594.
14 J. K. Feng, M. O. Lai and L. Lu, *Electrochem. Commun.*, 2011, **13**, 287.
15 R. Yi, J. Feng, D. Lv, M. L. Gordin, S. Chen, D. Choi and D. Wang, *Nano Energy*, 2013, **2**, 498.

16 F. Zou, X. Hu, Y. Sun, W. Luo, F. Xia, L. Qie, Y. Jiang and Y. Huang, *Chem. Eur. J.,* 2013, **19**, 6027.
17 W. Li, X. Wang, B. Liu, J. Xu, B. Liang, T. Luo, S. Luo, D. Chen and G. Shen, *Nanoscale*, 2013, **5**, 10291.
18 F. Zou, X. Hu, L. Qie, Y. Jiang, X. Xiong, Y. Qiao and Y. Huang, *Nanoscale*, 2014, **6**, 924.
19 W. Chen, L. Lu, S. Maloney, Y. Yang and W. Wang, *Phys. Chem. Chem. Phys.,2015,* **17**, 5109.
20 W. Chen, S. Maloney and W. Wang, *Electrochim. Acta*, 2015, **176**, 96.
21 X. Li, Y. Feng, M. Li, W. Li, H. Wei and D. Song, *Adv. Funct. Mater.*, 2015, **25**, 6858.
22 Y. Feng, X. Li, Z. Shao and H. Wang, *J. Mater. Chem. A*, 2015, **3**, 15274.
23 Q. Li, X. Miao, C. Wang and L. Yin, *J. Mater. Chem. A*, 2015, **3**, 21328.
24 A. Rong, X. P. Gao, G. R. Li, T. Y. Yan, H. Y. Zhu, J. Q. Qu and D. Y. Song, *J. Phys. Chem. B*, 2006, **110**, 14754.
25 X. J. Zhu, L. M. Geng, F. Q. Zhang, Y. X. Liu and L. B. Cheng, *J. Power. Sources*, 2009, **189**, 828.
26 X. Hou, Q. Cheng, Y. Bai and W. F. Zhang, *Solid State Ionics,* 2010*,* **181**, 631.
27 J. –W. Lee and C. –H. Lee, *J. Supercrit. Fluid.,* 2010, **55**, 252.
28 N. Feng, S. Peng, X. Sun, L. Qiao, X. Li, P. Wang, D. Hu and D. He, *Mater. Lett.,* 2012, **76**, 66.
29 C. T. Cherian, M. Zheng, M. V. Reddy, B. V. R. Chowdari and C. H. Sow, *ACS Appl. Mater. Inter.*, 2013, **5**, 6054.
30 W. Song, J. Xie, W. Hu, S. Liu, G. Cao, T. Zhu and X. Zhao, *J. Power. Sources,* 2013, **229**, 6.
31 Y. Zhao, Y. Huang, W. Zhang, Q. Wang, K. Wang and M. Zong, *RSC Adv.*, 2013, **3**, 23489.
32 H. Huang, Y. Huang, M. Wang, X. Chen, Y. Zhao, K. Wang and H. Wu, *Electrochim. Acta,* 2014, **147**, 201.
33 H. Fan, Z. Liu, J. Yang, C. Wei, J. Zhang, L. Wu and W. Zheng, *RSC Adv.,* 2014, **4**, 49806.
34 Y. Zhao, Y. Huang, X. Sun, H. Huang, K. Wang, M. Zong and Q. Wang, *Electrochim Acta,* 2014, **120**, 128.
35 R. Zhang, Y. He and L. Xu, *J. Mater. Chem. A,* 2014, **2**, 17979.
36 Y. Zhao, Y. Huang, Q. Wang, K. Wang, M. Zong, L. Wang and X. Sun, *Ceram Int.,* 2014, **40**, 2275.
37 B. –Y. Wang, H. –Y. Wang, Y. –L. Ma, X. –H. Zhao, W. Qi and Q. –C. Jiang, *J. Power. Sources*, 2015, **281**, 341.
38 H. –Y. Wang, B. –Y. Wang, J. –K. Meng, J. –G. Wang and Q. –C. Jiang, *J. Mater. Chem. A*, 2015, **3**, 1023.
39 Y. Sharma, N. Sharma, G. V. S. Rao and B. V. R. Chowdari, *Adv. Funct. Mater.*, 2007, **17**, 2855.
40 G. Zhang, S. Hou, H. Zhang, W. Zeng, F. Yan, C. C. Li and H. Duan, *Adv. Mater.*, 2015, **27**, 2400.
41 Shilpa, B. M. Basavaraja, S. B. Majumder and A. Sharma, *J. Mater. Chem. A*, 2015, **3**, 5344.
42 N. Yabuuchi, K. Kubota, M. Dahbi and S. Komaba, *Chem. Rev.*, 2014, **114**, 11636.
43 D. Kundu, E. Talaie, V. Duffort and L. F. Nazar, *Angew. Chem. Int. Ed.*, 2015, **54**, 3431.
44 V. L. Chevrier and G. Ceder, *J. Electrochem. Soc.*, 2011, **158**, A1011.
45 L. Baggetto, J. K. Keum, J. F. Browning and G. M. Veith, *Electrochem. Commun.*, 2013, **34**, 41.
46 P. R. Abel, Y. –M. Lin, T. D. Souza, C. –Y. Chou, A. Gupta, J. B. Goodenough, G. S. Hwang, A. Heller and C. B. Mullins, *J. Phys. Chem. C*, 2013, **117**, 18885.
47 A. Kohandehghan, K. Cui, M. Kupsta, J. Ding, E. M. Lotfabad, W. P. Kalisvaart and D. Mitlin, *Nano Lett.*, 2014, **14**, 5873.
48 Y. Xu , Y. Zhu, Y. Liu and C. Wang, *Adv. Energy Mater.*, 2013, **3**, 128
49 D. –H. Nam, T. –H. Kim, K. –S. Hong and H. –S. Kwon, *ACS Nano*, 2014, **8**, 11824.
50 J. Liu, Y. Wen, P. A. V. Aken, J. Maier and Y. Yu, *Nano Lett.*, 2014, **14**, 6387.
51 M. F. Oszajca, M. I. Bodnarchuk and M. V. Kovalenko, *Chem. Mater.*, 2014, **26**, 5422.
52 Z. Li, J. Ding and D. Mitlin, *Acc. Chem. Res.,* 2015*,* **48**, 1657.
53 Y. Zhang , P. Zhu, L. Huang, J. Xie, S. Zhang, G. Cao and X. Zhao, *Adv. Funct. Mater.*, 2015, **25**, 481.
54 Y. Liu, N. Zhang, L. Jiao and J. Chen, *Adv. Mater.*, 2015, **27**, 6702.
55 Z. Li, J. Ding, H. Wang, K. Cui, T. Stephenson, D. Karpuzov and D. Mitlin, *Nano Energy*, 2015, **15**, 369.
56 Q. Liu, Y. Zhou, J. Kou, X. Chen, Z. Tian, J. Gao, S. Yan and Z. Zou, *J. Am. Chem. Soc.,* 2010, **132**, 14385.
57 Z. Li, Y. Zhou, C. Bao, G. Xue, J. Zhang, J. Liu, T. Yu and Z. Zou, *Nanoscale,*2012, **4**, 3490.
58 H. S. Im, Y. J. Cho, Y. R. Lim, C. S. Jung, D. M. Jang, J. Park, F. Shojaei and H. S. Kang, *ACS Nano*, 2013, **7**, 11103.

## Entry for the Table of Contents

Text for Table of Contents

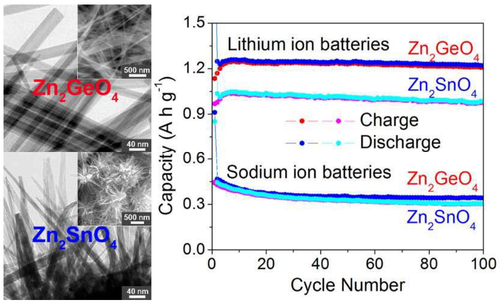


$Zn_2GeO_4$ and $Zn_2SnO_4$ nanowires showed an excellent cycling performance for both lithium- and sodium-ion batteries.